Stress evolution following the 1999 Chi-Chi, Taiwan, earthquake: Consequences for afterslip, relaxation, aftershocks, and departures from Omori decay

Chung-Han Chan[1,3] and Ross S. Stein[2]

[1]GeoForschungZentrum Potsdam, Section 5.3 Engineering Seismology, Germany
[2]U. S. Geological Survey, Menlo Park, California, USA

Abstract. We explore how Coulomb stress transfer and viscoelastic relaxation control afterslip and aftershocks in a continental thrust fault system. The 21 September 1999 M_w=7.6 Chi-Chi shock is typical of continental ramp-décollement systems throughout the world, and so inferences drawn from this uniquely well-recorded event may be widely applicable. First, we find that the spatial and depth distribution of aftershocks and their focal mechanisms are consistent with the calculated Coulomb stress changes imparted by the coseismic rupture. Some 67% of the M≥2 aftershocks and 83% of the M≥4 aftershocks lie in regions for which the Coulomb stress increased by ≥0.1 bars, and there is a 11-12% gain in the percentage of aftershocks nodal planes on which the shear stress increased over the pre-Chi Chi control period. Second, we find that afterslip occurred where the calculated coseismic stress increased on the fault ramp and décollement, subject to the condition that friction is high on the ramp and low on the décollement. Third, viscoelastic relaxation is evident from the fit of the postseismic GPS data on the footwall. Fourth, we find that the rate of seismicity increased about a year after Chi-Chi in an annulus extending east of the main rupture. The spatial extent of the seismicity annulus resembles the calculated ≥0.05-bar Coulomb stress increase caused by viscoelastic relaxation and afterslip, and we find a 9-12% gain in the percentage of focal mechanisms with >0.01-bar shear stress increases imparted by the postseismic afterslip and relaxation in comparison to the control period. Thus, we argue that postseismic stress

[3]Formerly at Institute of Geophysics, National Central University, Chung-Li, Taiwan

changes can for the first time be shown to alter the production of aftershocks, as judged by their rate, spatial distribution, and focal mechanisms.

1. Introduction

Many studies have examined the hypothesis that static stress changes influence the spatial or temporal distribution of aftershocks and subsequent large shocks (see reviews by *Harris*, 1998, *Stein*, 1999, *King and Cocco*, 2000, *Freed*, 2005, and *Steacy et al*, 2005). However, only few such studies have analyzed large thrust earthquakes (*Parsons*, 2002; *Lin and Stein*, 2004; *Ma et al*, 2005), and fewer still benefit from the rich seismic catalog (*Chang et al*, 2000), and dense GPS (*Yu et al*, 2001) and accelerometer (*Ma et al*, 2001) networks in Taiwan.

Ma et al (2005) argued that the Chi-Chi event exhibits unequivocal evidence of Coulomb stress transfer in promoting aftershocks, with increases and decreases in the M≥2 seismicity rate corresponding to calculated Coulomb stress change, although the seismicity rate decreases in the Coulomb stress shadows do not become evident until 2-3 months after the mainshock. The Chi-Chi mainshock was calculated to promote failure on the rupture planes of most M≥4 aftershocks, and nearly all of the ten M≥6 aftershocks that struck within the first year were found to be promoted by several bars by the coseismic stresses. In addition, for large events such as Chi-Chi, afterslip, lower crust-upper mantle viscoelastic rebound, and large aftershocks themselves may cause measurable postseismic deformation (*Rundle and Jackson*, 1977; *Thatcher*, 1983; *Savage*, 1990), which we study here. The 7 continuous and 80 campaign GPS stations of Taiwan also provide an unprecedented opportunity to study the postseismic deformation following the Chi-Chi earthquake.

Here we investigate the role of the coseismic stresses in promoting the afterslip, and we test whether stresses imparted by the afterslip and viscoelastic rebound modified the distribution and

decay of aftershocks. Although many studies have proposed such a mechanism (Pollitz et *al*, 2004; *Freed*, 2005; *Freed et al*, 2007), none has demonstrated a change in the aftershock migration, distribution or rate corresponding to relaxation or afterslip.

2. Models and methods

2.1 Coseismic and postseismic slip models derived from GPS observations

We calculate the Coulomb stress changes for Chi-Chi coseismic slip models obtained by *Johnson and Segall* (2004) (Figure 1a). The several studies that have illuminated the kinematics of the Chi-Chi rupture process (e.g*., Ma et al*, 1999; *Ma et al*., 2001; *Zeng and Chen*, 2001; *Chi et al*., 2001; *Ji et al*., 2003; *Johnson and Segall*, 2004; *Perfettini and Avouac*, 2004) contain consistent features, such as large coseismic displacements in the northern portion of the Chelungpu fault. *Johnson and Segall* (2004) employ a four-plane fault geometry with a sub-horizontal décollement located at ~8 km depth to explain the significant GPS deformation observed in central Taiwan (Figure 2a). Due to the paucity of GPS stations southeast of the epicenter, the quality of the model becomes questionable over the southeastern part of the décollement.

We use the afterslip model of *Yu et al*. (2003), which attributes the first 15 months of observed GPS displacements exclusively to afterslip (Figure 1b and Figure 2b). Slip is resolved on four planes with a sub-horizontal décollement located at ~10 km depth, covering a much larger area than the coseismic model (Figure 1c). *Yu et al*. find two slip asperities, downdip from the mainshock hypocenter and another to the south of the coseismic slip. By contrast, to the north where the maximum coseismic displacement occurred, the inferred afterslip is relatively modest.

The *Yu et al*. model fits the GPS data on the hanging wall quite well, but systematically misfits the footwall observations (Figure 2b). Because the hanging wall displacements are generally about 4 times larger than those on the footwall, models that minimize the combined rms residuals

need not satisfy the footwall deformation despite the large number of footwall GPS stations. Only two GPS stations (S027 and YUSN in Figure 2b) constrain the location, size and slip in the southern asperity of *Yu et al*. Since displacements of ~10 cm at these stations are significant, slip to the south of the coseismic rupture is required, but its location and the slip minima between the northern and southern patches poorly determined.

2.2 Viscoelastic deformation model

We employ VISCO1D (*Pollitz*, 2006) in a spherical layered earth with the viscosity structure (Figure 3c). Based on interseismic GPS data, *Johnson et al* (2005) inferred a high asthenospheric viscosity (2.0×10^{19} Pa s) throughout Taiwan except perhaps beneath Central Range, where the viscosity could be lower (*Sheu and Shieh*, 2004; *Hsu*, 2004). With the assumed structure we explore the contribution of viscoelastic deformation to the observed GPS displacements and Coulomb stress changes. The surface displacements from viscoelastic deformation greatly reduces the GPS residuals in the footwall 10-25 km from the Chelungpu fault (blue shaded area in Figure 3a). Over the décollement and in the hanging wall, however, the observed displacements are dominated by afterslip (Figure 2b), and the calculated viscoelastic deformation is modest (Figure 3b). Thus, while viscoelastic deformation is more subtle than afterslip, both processes are likely active.

Neither the afterslip model of *Yu et al* (2003) nor viscoelastic deformation satisfies the observed GPS displacements within 5-10 km of the Chelungpu fault on the footwall block (yellow shaded area in Figure 3a). A possible explanation for this misfit could be about 15 cm of postseismic slip on the Changhua fault (blue line in Figure 3a).

2.3 Methods

We calculate the Coulomb failure stress (ΔCFS) resolved onto specified fault planes inferred from focal mechanisms of M≥4 aftershocks, in which $\Delta CFS = \Delta\tau + \mu'\Delta\sigma$, where $\Delta\tau$ is the shear

stress change, μ' is effective friction coefficient, and $\Delta\sigma$ is the unclamping (or normal) stress change (*King et al*., 1994; *Toda et al*., 1998). Generally μ' is modeled in most studies to lie between 0.4 and 0.8. However, there is evidence that highly lubricated faults or those with large cumulative slip such as the central San Andreas fault may have $\mu'<0.2$ (*Zoback et al*, 1987; *Toda & Stein*, 2003), whereas jagged, anastomosing faults with rough or cohesive surfaces and little cumulative slip can have $\mu'>0.8$ (*Parsons et al*, 1999; *Lin & Stein*, 2004). We also tested the assumption of constant friction against the isotropic poroelastic assumption in computing Coulomb stress changes (*Beeler et al*., 2000; *Cocco and Rice*, 2002), but for reasonable values of dry friction (0.75) and Skempton's coefficients (0.5-0.9), the results were indistinguishable from each other.

Although driven by a uniform NW-SE regional tectonic stress (*Seno*, 1977; *Hu et al.*, 1996), Taiwan is traversed by high-angle reverse and ramp faults, décollements, and strike-slip faults over a range of depths (*Seno*, 1977; *Suppe*, 1985; *Kao and Chen*, 2000; *Chi and Dreger*, 2004). The diversity of faulting styles is reflected in the focal mechanisms, and for this reason we resolve the Coulomb stress change on several types of 'receiver faults' such as on the nodal planes of focal mechanisms or on fault surfaces in their rake directions.

3. Coulomb stress calculations

3.1 Stress change for an idealized ramp-décollement model

Because the geometry and slip distribution of the Chi-Chi earthquake are complex, we first illustrate the stress transferred by a simplified Chi-Chi earthquake on an idealized ramp-flat thrust fault system (Figure 4). While the coseismic slip was greater on the ramp, afterslip is inferred by *Yu et al* (2003) to be greater on the décollement, and so these distributions are reflected in the idealizations. In addition, most focal mechanisms of the Chi-Chi aftershocks are both thrust and

strike-slip, and so the coseismic stress changes are resolved on both types of receiver planes. For 30°-dipping thrust faults (upper panels of Figure 4), the coseismic slip drops the stress throughout the upper 15 km, or much of the seismogenic depth.

Since much of the background seismicity occurs on north-striking left-lateral faults (*Seno*, 1977; *Hu et al*, 1996; *Ma et al*, 2005), we resolve the stress changes on these receiver planes in the lower panels of Figure 4. The afterslip tends to re-load parts of the upper crust (Figure 4j). Unlike the pattern for thrust receivers, the stress transfer to strike-slip receiver faults shows an antisymmetrical distribution, which arises because the rake of the source fault is perpendicular to the rake of the receivers (Figure 4d and Figure 4i).

3.2 Association of aftershocks with coseismic stress changes

We next calculate the Coulomb stress change using the full *Johnson and Segall* (2004) coseismic model. Because the majority of the aftershock focal mechanisms are consistent with low-angle thrust slip (Figure 5a), we use receiver fault planes similar to in the idealized Figure 4a-b, consistent with the Chi-Chi mainshock: 30°-dipping thrust faults striking parallel to the Chelungpu fault with rakes of 80°. The resemblance between the idealized and detailed models is evident (Figure 4a and Figure 5b-c), with the exception that in Figure 5b-c, we show the maximum Coulomb stress change over a depth range rather than at one depth. In Figure 5, we also use different receiver faults in the two boxed regions dominated by oblique (Pakuashan) and strike-slip (Fengshan) mechanisms. These assignments are based on the identified focal mechanism of the largest aftershock in each region, and the fault plane is distinguished from the nodal plane from seismicity alignments evident in Figure 5a. Some 67% of M≥2 shocks and 83% of M≥4 earthquakes (denoted in the figure by focal mechanisms) lie in regions of Coulomb stress increases of ≥0.1 bar for the assumed receiver fault orientations indicated in Figure 5a. Some 52% of the aftershocks above

the décollement (Figure 5b) and 75% of those below (Figure 5c) lie in regions of calculated ≥0.1-bar Coulomb stress changes. We also resolve the Coulomb stress change on the BATS focal mechanisms shown in Figure 5a; the stress increased by ≥0.1 bar on 83% of the focal planes.

To further compare the Coulomb stress change and aftershocks, five cross-sections are presented in Figure 6 along the routes shown in Figure 5b-c. Here the stress is resolved on the dominant local mechanism, which in most cases is a low-angle thrust fault. Some 74% of the focal mechanisms of M≥4 aftershocks lie in regions of ≥0.1 bar Coulomb stress increase. Nevertheless, many M≥2 aftershocks lie above the décollement, where the Coulomb stress on 30°-dipping thrust faults is calculated to have decreased. These earthquakes would only be consistent with stress transfer if they struck on faults with different orientations, such as horizontal décollements (as shown for the idealized Chi-Chi rupture in Figure 4c). Because we lack focal mechanisms for Most of the M≥2 shallow aftershocks, this question is unresolved.

3.3 Stress change on aftershock nodal planes

As an alternative assessment of the efficacy of the stress changes in promoting aftershocks we examine the percentage of aftershock nodal planes with stress increased by the coseismic slip (Figure 7, solid lines), following *Hardebeck et al* (1998). Because of the nodal plane uncertainty for the aftershocks, this calculation is unambiguous only for the shear stress change, or if we assume the friction is very low. What matters in these comparisons is the gain in the percentage of positively stressed mechanisms, which is tallied to the right of the graph, rather than the absolute numbers. We compare the percentage of stress increases on focal mechanisms during the 53-month period before Chi-Chi (the control period) to the period 3-15 months after the Chi-Chi mainshock (the test period), and find a 12% gain for aftershocks with shear stress increases >0.1 bars (Figure 7a), and a 11±3% gain for Coulomb stress increase of ≥0.1 bars (Figure 7c). For the

Coulomb stress changes, we assume μ=0.4, and randomly choose one nodal plane of each pair in 10 realizations, and then report the mean and standard deviation. We use the period 3-15 months post-Chi Chi because *Ma et al* (2005) found that the first 3 months did not show seismicity rate drops in the stress shadows and so might be dominated by dynamic stress or shaking effects, and because postseismic surveys conducted 15 months after the mainshock were used to develop the afterslip model.

Thus this study and its forerunner, *Ma et al* (2005), demonstrate that even when the source geometry and slip distribution are complex, Coulomb stress transfer is correlated with the distribution of aftershocks and their focal mechanisms. The next question we tackle is whether the stresses also govern the afterslip.

3.4 Coseismic stress change resolved on the postseismic surface

To understand the influence of coseismic stress change on afterslip, we calculate the stress imparted by the coseismic slip of the *Johnson and Segall* (2004) (Figure 8) on the ramp and décollement. This calculation would be straightforward if the afterslip occurred exclusively off the coseismic rupture, such as on its downdip or along-strike extensions. But parts of the coseismic slip surface are inferred by *Yu et al* (2003) to have slipped further during the postseismic period, and the coseismic slip discontinuities cause large local stress changes on the fault. We thus smoothed the stress changes with a Gaussian nearest-neighbor filter, iterated the number of times specified in Table 1. *Johnson and Segall* (2004) use an 8-km depth for the décollement, whereas *Yu et al* (2003) use 10 km. The difference is beyond the resolution of the geodetic data, and so we calculate stress changes within a layer extending 3 km above and below the décollement. The resulting stress changes are still far from smooth, making comparisons of coseismic stress to afterslip qualitative.

The coseismic slip causes a shear stress increase downdip of the hypocenter, and a shear stress decrease on the upper 5 km of the ramp (Figure 8b). Afterslip apparently extends nearly to the ground surface, where the coseismic slip is calculated to cause unclamping and a shear stress decrease (Figure 8b-c). We find a positive correlation between coseismic shear stress increase and postseismic slip on 60% of the décollement surface; a positive correlation is found between coseismic unclamping and postseismic slip on 67% of the ramp surface.

The Coulomb stress changes imparted by the coseismic slip could thus have at least partly driven the afterslip if the effective friction on the décollement surface, μ', were very low. Independent evidence suggests that because décollement surfaces are not optimally aligned in a compressive tectonic regime, they can only slip if they possess very low friction, caused either by layer interbeds, extensive gouge zones, or high pore fluid pressure (*Barr and Dahlen*, 1989; *Byrne and Fisher*, 1990), and so this inference may be reasonable.

3.5 Postseismic stress change associated with postseismic seismicity

Next we seek to understand whether stress changes induced by the afterslip and postseismic deformation alter the seismicity rate and its distribution. In other words, to what extent is the aftershock sequence anomalous once afterslip and viscoelastic relaxation have progressed. To isolate aftershocks with a decaying frequency from the presumably more steady background seismicity, we create a projected aftershock rate map using earthquakes above the magnitude of completeness, M_c. For the 50-month pre- and post-Chi Chi periods, $M_c \leq 2$ in the interior of Taiwan; $M_c \leq 3$ for regions within about 100 km of the coastline (*Ma et al.*, 2005). To capture a sufficient number of earthquakes with these magnitudes, we use 50 x 50 km cells.

We first subtract the 50-month pre-Chi Chi seismicity rate from the rate observed during the first 3 months of aftershocks to remove the steady background seismicity. This step is important

for sites far from the Chi-Chi mainshock where the background rate is high and there are few aftershocks. We then fit the decay in each cell to the 3-15 month residuals, using modified Omori's law (*Utsu*, 1961), solving for the decay exponent *p,* which is generally found to be about -1.0, and for the *c* term in $n(t)=k/(c+t)^p$, where *n* is the number of aftershocks in a cell. A representative time series for one cell is shown in Figure 9b. In Figure 10, we plot the seismicity rate change, the ratio of the rate 15-53 months to 3-15 months after the Chi-Chi earthquake. The resulting *p* values are given for each cell. Because we are taking a ratio of late to early aftershock rates, the productivity term *k* falls out; since *c* is thought to originate from catalog incompleteness immediately after the mainshock, we do not report it here. Sites with $p\sim1$, which extend up to 100 km from the fault, experienced a rapid decay of aftershock frequency during the first 3 months. Sites with $p\sim0$ exhibited steady seismicity rates with no discernable aftershocks.

The observed late aftershock sequence is shown in Figure 10b; this is simply the observed ratio of the rate 15-53 months to 3-15 months after the Chi-Chi mainshock. The distribution shows a broad seismicity rate drop in central Taiwan region centered on the Chi-Chi décollement, consistent with aftershock decay during the first 15 months (Figure 10a). However, there is a semi-annulus of seismicity rate increases extending east of the mainshock labeled 'E. offshore annulus' in Figure 10b, as well as a cell 50 km north of the northern end of the fault rupture which also experienced a seismicity rate increase. Only 3-4 of the 12 cells with observed increases are associated with $M\geq6$ shocks that occurred 15-53 months after the mainshock.

The observed departure from Omori decay resembles the calculated stresses imparted by afterslip and relaxation in Figure 10c-d, particularly for regions off the main fault rupture. The East offshore annulus is expected to be the site of thrust earthquakes, and both thrust and strike-slip faults should experience stress increases both northeast and north of the rupture, in accord with the observed seismicity rate increases (Figure 10b) and observed focal mechanisms (Figure 10c-d).

The target depth of 20 km used in Figure 10c-d is consistent with the average depth of earthquake hypocenters. The depth and focal mechanism-dependence of these patterns can be judged from idealized cross-sections of Figure 4g and Figure 4j. The offshore seismicity increase was accompanied by four M≥6 shocks; these shocks could have been promoted by the stress increase, and they undoubtedly contribute to the seismicity rate increase. The decrease in Coulomb stress over the décollement is also evident in Figure 10c-d.

There is fair correspondence between the calculated postseismic Coulomb stress changes with focal mechanisms in Figure 10c-d, with 59% of the strike-slip mechanisms and 73% of the thrust mechanisms after December 2000 occurring in regions of expected Coulomb increase. Further, the Coulomb stress change on strike-slip faults is increased in 54% of the area in East Offshore annulus by postseismic processes, and 76% of the annulus is enhanced for thrust faults. Table 2 gives the shear stress change on the M>5.5 mechanisms that took place after the first 15 months; since the fault plane cannot be distinguished from the nodal plane, the unclamping stress is ambiguous and so the Coulomb stress is uncertain. About 57% of these events are calculated to have sustained coseismic+postseismic shear stress increases.

We also tested the percent of aftershock focal mechanisms with shear stress increases imparted by the afterslip and relaxation, and find increases of 9-12% over the pre-Chi Chi control period (Figure 7a-b, dashed lines). In Figure 7a-b, it is also evident that the percentage of encouraged mechanisms increases with time following the mainshock, as would be expected since afterslip and relaxation occur over a period longer than 15 months. In contrast, the percentage of mechanisms encouraged by the coseismic stresses drops by 4-10% after the first 15 months (Figure 7a-b, solid lines), indicating that the stresses evolve over time. For the Coulomb stress the increase is not significant (3±3%) perhaps because of the nodal plane ambiguity, or because fault friction is lower than the tested value of 0.4 (Figure 7c, dashed lines).

4. Discussion and Conclusions

4.1 Coseismic and postseismic slip in crustal unloading and reloading

Stress is imparted to the crust surrounding the Chelungpu fault from three sources: the coseismic slip, aftershocks, and postseismic processes including afterslip and relaxation. The relative magnitudes of these sources can be gauged in Figure 11, which makes clear that afterslip alone contributes more seismic moment than aftershocks. Afterslip carries 3.5 the moment of the largest (M≥6) aftershocks. Including M≥4 shocks increases the moment of the aftershocks by 15%, to 1.7 x 10^{19} Nm. For a *b*-value near 1, afterslip contributes about 2.5 times the moment of all aftershocks.

The Coulomb stress imparted by slip on a ramp-décollement system is quite unlike that of a continental blind thrust fault (*Lin and Stein*, 2004) or subduction megathrust (*Hsu et al*, 2006) because the upper crust (<8-10 km depth) is brought farther from failure while the the crust beneath the décollement is brought closer to failure (Figure 4b). Afterslip on the décollement acts to reload the upper crust (Figure 4g). In contrast, blind thrust faults without décollements tend to increase the failure stress in the upper crust coseismically, producing diffuse and highly productive aftershock sequences (*Lin and Stein*, 2004).

4.2 Role of Coseismic slip in controlling aftershocks

Extending the study of *Ma et al* (2005), we find that the coseismic Coulomb stress changes are correlated with the distribution of aftershocks both in map view (Figure 5) and cross-section (Figure 6). The analysis is complicated by the diversity of focal mechanisms and faulting regimes, but when we resolve stresses on planes corresponding to the principal focal mechanisms in each region, the association of seismicity and calculated Coulomb stress change is evident with correla-

tion coefficients spanning 49-94%. Calculating the stress imparted to aftershock nodal planes, we find that the percentage of focal mechanisms for which the Coulomb stress increased by ≥0.1 bar as a result of the mainshock rose by 11±3% over a control period before the mainshock (Figure 7).

4.3 Co-location of afterslip with décollement seismicity

As reported by *Yu et al* (2003), afterslip extends downdip from the peak coseismic slip, covering a larger area of the décollement. During the period of measured afterslip, aftershocks are concentrated where the afterslip is high (Figure 1b). This zone of seismicity is also at the periphery of the coseismic slip (Figure 5a), and so it is not clear whether aftershocks occur where the stress imparted by the coseismic slip is high, or where the afterslip is high, or both.

4.4 Role of low décollement friction in promoting afterslip

We argue that the coseismic stress changes drive the occurrence of afterslip. While we have used an intermediate value for the fault friction of $\mu'=0.4$ for the stress resolved on nodal planes of M≥4 focal mechanisms, we find that slip on the décollement and the base of the ramp is best correlated with the shear stress change, implying $\mu'\sim0.0$ (Figure 8). Thus because a horizontal surface must be profoundly weak to slip, the décollement may exhibit unique properties in comparison to the surrounding crust.

4.5 Simultaneous and viscoelastic deformation processes

Departing from *Yu et al* (2003), we argue that the postseismic GPS displacements on the footwall are systematically misfit by afterslip alone. When viscoelastic relaxation is also included, the footwall residuals are greatly reduced (Figure 3), and the hanging-wall residuals are little affected. Relaxation is not confined to the footwall; rather, over the décollement surface GPS displacements from afterslip dwarf displacements associated with relaxation. In subduction zones,

the footwall is under water and so its deformation is never measured, rendering the most distinctive signal of relaxation unobtainable for most megathrust earthquakes.

4.6 Aftershock decay departs from the initial distribution following afterslip and relaxation

After most of the measured afterslip had taken place, the observed aftershock rates departed from that projected from the initial 3 months of decay. The seismicity rate offshore the eastern coastline and north of the fault rupture increased, incompatible with—or unrelated to—Omori decay (Figure 10b). The observed increases correspond spatially to the stresses imparted by afterslip and relaxation (Figure 10c-d), and the percentage of focal mechanisms brought closer to failure by the afterslip and relaxation rose by 9-12% over a control period before the mainshock (Figure 7). The M≥4 aftershocks beginning 15 months after the Chi-Chi mainshock are correlated with the calculated Coulomb stress changes imparted by viscoelastic relaxation and afterslip at the level of 59-73% (Figure 10c-d).

Acknowledgements. We thank Fred Pollitz for guidance in the use and interpretation of VISCO1D, Shinji Toda for providing Coulomb 3.1, and Jeanne Hardebeck, Kuo Fong Ma, Volkan Sevilgen, Massimo Cocco, Rodolfo Console, and Sandy Steacy for thoughtful reviews. We thank the National Science Council of Taiwan for a C.-H.C.'s Fellowship to spend a year at the USGS.

References

Barr, T.D., and Dahlen, F. A., Brittle frictional mountain building, 2. Thermal structure and heat budget, *J. Geophys. Res*., **94**, 3923-3947, 1989.

Beeler, N., R. Simpson, S. Hickman, and D. Lockner, Pore fluid pressure, apparent friction, and Coulomb failure, *J. Geophys. Res*., **105**, 25533-25542, 2000.

Byrne, T., and D. Fisher, Evidence for a weak and overpressured décollement beneath sediment dominated accretionary prisms, *J. Geophys. Res*., **95**, 9081–9097, 1990.

Chan, C.-H., K.-F. Ma, Possibility of Forecasting Aftershock Distributions from Stress Change: A Case Study of Inland Taiwan Earthquakes. *Terr., Atmo. and Ocea. Scie*., **15**, 503-521, 2004.

Chang, C.- H., Y.- M. Wu, T.- C. Shin and C.- Y. Wang, Relocation of the 1999 Chi-Chi Earthquake in Taiwan. *Terr. Atmos. Oceanic Sci.,*, **11(3)**, 581-590, 2000.

Chi, W.-C., D. Dreger, and A. Kaverina, Finite-source modeling of the 1999 Taiwan (Chi-Chi) earthquake derived from a dense strong motion network, *Bull. Seism. Soc. Am.*, **91**, 1144– 1157, 2001.

Cocco, M. and J. Rice, Pore pressure and poroelasticity effects in Coulomb stress analysis of earthquake interactions, *J. Geophys. Res*., **107**, NO. 0, 10.1029/2000JB000138, 2002.

Freed, A. M., Earthquake triggering by static, dynamic, and postseismic stress transfer, *Annu. Rev. Earth Planet. Sci.*, **2005**.33:335–67, doi: 10.1146/annurev.earth.33.092203.122505, 2005.

Freed, A. M., S. T. Ali, and R. Bürgmann, Evolution of stress in Southern California for the past 200 years from coseismic, postseismic and interseismic stress changes, *Geophys. J. Int*. **169**, 1164–1179 doi: 10.1111/j.1365-246X.2007.03391.x, 2007.

Hardebeck, J. L., J. J. Nazareth, and E. Hauksson, The static stress change triggering model: Constraints from two southern California aftershocks sequences, *J. Geophys. Res.*, 103, 24,427–24,437, 1998.

Harris, R. A. (1998), Introduction to special section: Stress triggers, stress shadows, and implications for seismic hazard, *J. Geophys. Res.*, *103*, 24,347-324,358.

Hsu, Y.-J., Modeling studies on interseismic, coseismic and postseismic deformations associated with the 1999 Chi-Chi, Taiwan earthquake, Ph. D. Dissertation, 112 pp., *Natl. Cent. Univ.*, Taiwan, 2004.

Hu, J.-C., J. Angelier, J.- C. Lee, H.- T. Chu, and D. Byrne, Kinematics of convergence, deformation and stress distribution in the Taiwan collision area: 2-D Finite-element numerical modeling, *Tectonophysics*, **255**, 243-268, 1996.

Ji, C., D. V. Helmberger, D. J. Wald, and K.-F. Ma, Slip history and dynamic implications of the 1999 Chi-Chi, Taiwan, earthquake, *J. Geophys. Res.*, 108, 2412, doi:10.1029/2002JB001764, 2003.

Johnson, K .M., and P. Segall, Imaging the ramp–décollement geometry of the Chelungpu fault using coseismic GPS displacements from the 1999 Chi-Chi, Taiwan earthquake, *Tectonophys.,* **378**. 123-139*,* 2004.

Johnson, K. M., P. Segall, and S. B. Yu, A viscoelastic earthquake cycle model for Taiwan, *J. Geophys. Res.*, **110**, doi:10.1029/2004JB003516, 2005.

Kao, H. and W.-P. Chen, The Chi-Chi earthquake sequence: active, out-of-sequence thrust faulting in Taiwan, *Science*, **288**, 2346-2349, 2000.

Kao, H., Y.-H. Liu, W.-T. Liang, and W.-P. Chen, Source parameters of regional earthquakes in Taiwan: 1999 – 2000 including the Chi-Chi earthquake sequence*, Terr. Atmos. Oceanic Sci.,* **13**, 279– 298, 2002.

King, G. C. P., R. S. Stein, and J. Lin, Static stress changes and the triggering of earthquakes, *Bull. Seism. Soc. Am.*, **84**, 935-953, 1994.

King, G. C. P., and M. Cocco (2000), Fault interaction by elastic stress changes: New clues from earthquake sequences, *Advances in Geophysics*, *44*, 1-36.

Lee, T.-Y. and Lawver, L. A., Tectonic evolution of the South China Sea region. *J. Geol Soc. China*, **35**, 353-388, 1992.

Lin, A. T., A. B. Watts, and S. P. Hesselbo, Cenozoic stratigraphy and subsidence history South China Sea margin in the Taiwan region, *Basin Research*, **15**, 453–478, 2003.

Lin, C.-H., Thermal modeling of continental subduction and exhumation constrained by heat flow and seismicity in Taiwan. *Tectonophysics*, **324**,189–201, 2000.

Lin, J., R. S. Stein, Stress triggering in thrust and subduction earthquakes, and stress interaction between the southern San Andreas and nearby thrust and strike-slip faults, *J. Geophys. Res.*, **109**, B02303, doi:10.1029/2003JB002607, 2004.

Liang, W.-T., Y.-H. Liu, H. Kao, Source parameters of regional earthquakes in Taiwan: January-December 2001, *Terr., Atmos. and Ocean Sci.*, **14**, 249-260, 2003.

Liang, W.-T., Y.-H. Liu, H. Kao, Source parameters of regional earthquakes in Taiwan: January-December 2002, *Terr., Atmos. and Ocean. Sci*., **15**, 727-741, 2004.

Lin, J. and R.S. Stein, Stress triggering in thrust and subduction earthquakes, and stress interaction between the southern San Andreas and nearby thrust and strike-slip faults, *J. Geophys. Res.,* 109, B02303, doi:10.1029/2003JB002607, 2004.

Ma, K.-F., C.T. Lee, Y.B. Tsai, T.C. Shin, and J. Mori, The 1999 Chi-Chi, Taiwan (M_L=7.3, Mw=7.7) Earthquake – Large Surface Displacement on an Inland Thrust-fault, *EOS*, **80**, 605-611, 1999.

Ma, K.-F., J. Mori, S.-J. Lee, and S.-B. Yu, Spatial and temporal distribution of slip for the 1999 Chi-Chi, Taiwan earthquake, *Bull. Seism. Soc. Am.*, **91**, 1 – 19, 2001.

Ma, K.-F., C.-H. Chan, and R. S. Stein, Response of seismicity to Coulomb stress triggers and shadows of the 1999 Mw=7.6 Chi-Chi, Taiwan, earthquake, *J. Geophys. Res.*, **110**, doi:10.1029/2004JB003389, 2005.

Parsons, T., Global observation of Omori-law decay in the rate of triggered earthquakes: Large aftershocks outside the classical aftershock zone, *J. Geophys. Res.*, **107**, 2199, doi:10.1029/2001JB0006462, 2002.

Parsons, T., R. S. Stein, R. W. Simpson and P. A. Reasenberg, Stress sensitivity of fault seismicity: A comparison between limited-offset oblique and major strike-slip faults, *J. Geophys. Res.,* 104, 20,183-20,202, 1999.

Perfettini, H., J.-P. Avouac, Postseismic relaxation driven by brittle creep: A possible mechanism to reconcile geodetic measurements and the decay rate of aftershocks, application to the Chi-Chi earthquake, Taiwan, *J. Geophys. Res*., 109, B02304, doi:10.1029/2003JB002488, 2004

Pollitz, F. F., Transient rheology of the upper mantle beneath central Alaska inferred from the crustal velocity field following the 2002 Denali earthquake, *J. Geophys. Res.,* **110**, B08407, doi:10.1029/2005JB003672, 2005.

Pollitz, F. F., W. H. Bakun, and M. Nyst, A physical model for strain ac-cumulation in the San Francisco Bay region: Stress evolution since 1838, *J. Geophys. Res.*, **109**, B11408,

doi:10.1029/2004JB003003, 2004.

Pollitz, F. F., M. Nyst, T. Nishimura, and W. Thatcher, Inference of postseismic deformation mechanisms of the 1923 Kanto earthquake, *J. Geophys. Res., 111,* doi:10.1029/2005JB003901, 2006.

Rundle, J.B. & Jackson, D.D., A kinematic viscoelastic model of the San Francisco earthquake of 1906, *Geophys. J. R. Astr. Soc*., **50**, 441-458, 1977.

Savage, J.C., Equivalent strike-slip earthquake cycles in half-space and lithosphere-asthenosphere Earth models, *J. Geophys. Res.*, **95**, 4873-4879, 1990.

Seno, T, The instantaneous rotation vector of the Philippine Sea Plate relative to the Eurasian Plate, *Tectonophysics*, **42**, 209-226, 1977.

Sheu S.-Y., C.-F. Shieh, Viscoelastic-afterslip concurrence: a possible mechanism in the early post-seismic deformation of the Mw 7.6 1999 Chi-Chi (Taiwan) earthquake, *Geophys. J. Int*., **159**, 1112-1124, doi: 10.1111/j.1365-246X.2004.02437.x, 2004.

Shieh, C.-F., S.-Y. Sheu, and R.-C. Shih, Correlation between surface damage and the coseismic displacement and stress relaxation of the 1999 Chi-Chi, Taiwan earthquake *Geophys. Res. Lett.*, **28**, 3381-3384, 2001.

Suppe, J., *Principles of Structural Geology*, Prentice-Hall, Englewood Cliffs, 537 pp, 1985.

Steacy, S., J. Gomberg, M. Cocco, Introduction to special section: Stress transfer, earthquake triggering, and time-dependent seismic hazard, *J. Geophys. Res*., **110**, B05S01, doi:10.1029/2005JB003692, 2005.

Stein, R. S., The role of stress transfer in earthquake occurrence, *Nature*, **402**, 605-609, 1999.

Thatcher, W., Nonlinear strain build-up and the earthquake cycle on the San Andreas fault, *J. geophys. Res.*, **88**, 5893-5902, 1983.

Toda, S., R. S. Stein, P. A. Reasenberg, J. H. Dieterich, and A. Yoshida, Stress transferred by the Mw = 6.9 Kobe, Japan, shock: Effect on aftershocks and future earthquake probabilities. *J. Geophys. Res.*, **103**, 24543-24565, 1998.

Utsu, T., A Statistical Study on the Occurrence of Aftershocks, *The Geophysical Magazine*, **30(4)**, 521-605, 1961.

Waldhauser, F., W. L. Ellsworth, A double-difference earthquake location algorithm: Method and application to the northern Hayward fault, *Bull. Seism. Soc. Am.*, **90**, 1353-1368, 2000.

Wang, C.-Y., C.-L. Li, and H.-Y. Yen, Mapping the northern portion of the Chelungpu fault, Taiwan by shallow reflection seismics, *Geophys. Res. Lett.*, **29**, 1790, 10.1029/2001GL014496, 2002.

Wang, J.-H., Q value of Taiwan: a review, *J. Geol. Soc. China*, **36**, 15- 24, 1993.

Wang, W.-H., C.-H. Chen, Static stress transferred by the 1999 Chi-Chi, Taiwan, earthquake: effects on the stability of the surrounding fault systems and aftershock triggering with a 3D Fault-Slip Model, *Bull. Seismol. Soc. Am.,* **91***,* 1041-1052, 2001.

Wang, Y.-J., Three dimensional S-wave attenuation model of the crust and uppermost mantle beneath arc-continent collision, Taiwan, M.Sc. Dissertation, 112 pp., *Natl. Cent. Univ.*, Taiwan, 2004.

Wiemer, S., A software package to analyse seismicity: ZMAP, *Seismol. Res. Letts.*, **72 (3)**, 373-382, 2001.

Yu, S. B., L. C. Kuo, Y. J. Hsu, H. H. Su, C. C. Liu, C. S. Hou, J. F. Lee, T. C. Lai, C. C. Liu, C. L. Liu, T. F. Tseng, C. S. Tsai, and T. C. Shin, Preseismic deformation and coseismic displacements associated with the 1999 Chi-Chi, Taiwan earthquake, *Bull. Seismol. Soc. Am.,* **91***,* 995-1012, 2001.

Yu, S.-B., Y.-J. Hsu, L.-C. Kuo, and H.-Y. Chen, GPS measurement of postseismic deformation following the 1999 Chi-Chi, Taiwan, earthquake, *J. Geophys. Res.*, **108**, 2412, doi:10.1029/2003JB002396, 2003.

Zeng, Y. H., C. H. Chen, Fault rupture process of the 20 September 1999 Chi-Chi, Taiwan, earthquake, *Bull. Seismol. Soc. Am.,* **91** 1088–1098, 2001

Zoback, M.D., et al., New Evidence on the State of Stress of the San Andreas Fault System, *Science*, 238, 1105-1111, 1987.

Table Captions

Table 1. The number of smoothing passes specified on each fault surface in Figure 8. Every point is averaged with the value of its eight neighbors iteratively.

Table 2. The shear stress change resolved on the nodal planes of the M≥5.5 aftershocks that struck during the period 15-53 months after the Chi-Chi mainshock. Some 57% of shocks are associated with net coseismic plus postseismic shear stress increases, and 86% are associated with postseismic shear stress increases alone. The unclamping stress cannot be determined with confidence because of nodal plane ambiguity.

Figure captions

Figure 1. Coseismic slip distribution from (**a**) *Johnson and Segall* (2004) from geodetic data, with a thrust ramp and a horizontal décollement at depth of 7.7 km; the smaller rectangles are the northern segments (**b**) The 15-month afterslip distribution from *Yu et al.* (2003), with a ramp segment dipping 26˚ and a horizontal décollement at 10.4 km. The first 3 months of aftershocks occurring within 3 km of the rupture planes are shown as black dots. (**c**) Map-view of the model fault geometries; dashed rectangles correspond to the coseismic model; solid rectangles to the postseismic model.

Figure 2. (**a**) Horizontal GPS displacement residuals for the two coseismic models. (**b**) Observed and modeled displacements during first 15-month postseismic period after the Chi-Chi earthquake. Note lack of coverage in the southern part of the décollement.

Figure 3. Observed and modeled postseismic displacements. The footwall (**a**) and hanging wall (**b**) vectors are shown separately at different displacement scales. The inset is at the same spatial scale. Relaxation fits the footwall deformation more than 10 km from the fault well, but has no effect on the hanging wall, where the displacements are dominated by afterslip. Postseismic slip on the southern portion of the Changhua fault is also possible. (**c**) Rheology used for viscoelastic modeling, based on *Johnson et al* (2005) and *Pollitz* (2005).

Figure 4. Coulomb stress changes associated with an idealized Chi-Chi ramp-décollement rupture. (**a-c**) Coseismic stress changes, with higher slip on the ramp segment compared with décollement. The target depth of 15 km in **a** corresponds to the average depth of events in the first 3 months after the Chi-Chi earthquake. (**d-e**) Coseismic stress changes on north-striking left-lateral receiver faults. (**f-h**) Postseismic stress changes, with smaller slip on the ramp than the décollement, resolved on thrust faults. (**i-j**) Postseismic stress changes resolved on north-striking left-lateral receiver faults.

Figure 5. (a) Seismicity and focal mechanisms for the first 3 months after the Chi-Chi earthquake (Sep-Dec 1999), using the double-difference algorithm of *Waldhauser and Ellsworth* (2000). There are 1534 and 2895 M≥2.0 events above and beneath the décollement, respectively. The focal mechanisms were acquired by moment tensor inversion of waveforms recorded by the Broadband Array in Taiwan for Seismology (BATS) (*Kao et al.*, 2002). The star denotes the epicenter of the Chi-Chi mainshock. (**b**) Maximum coseismic Coulomb stress change over 0-7 km depth. (**c**) Maximum coseismic Coulomb stress change over 8-30 km depth. The black rectangles within green focal mechanisms mark the presumed fault planes on which stress is resolved in the Pakuashan and Fengshan regions. The Coulomb stress increased by ≥0.1 bar on 82% of the focal planes shown in (**a**).

Figure 6. Five cross-sections of the Coulomb stress change associated with the first 3 months of aftershocks and focal mechanisms within 5 km of each profile marked on Figure 5. Black lines denote the coseismic rupture fault geometry based on *Johnson and Segall* (2004). The strike/dip/rake of 3.3°/30°/80° is the Chi-Chi mainshock mechanism; other receiver fault orientations are based on the indicated focal mechanisms and the associated seismicity alignments in each panel. Section **a** lies north of the fault plane, amid strike-slip mechanisms aligned N80°W. In **c**, stress is resolved on the two receiver faults that correspond the local focal mechanisms, with a white vertical band dividing this composite section. The percentage of aftershocks in the ≥0.1-bar Coulomb stress change regions is given in the upper right of each panel.

Figure 7. Increase in the percentage of focal mechanisms with shear stress increases (**a**) >0.1 bars and (**b**) >0.01 bars, and (**c**) Coulomb stress increase >0.1 bar imparted by the coseismic (solid lines) and postseismic (short dashed lines) model.

Figure 8. (a) Afterslip model of *Yu et al.* (2003). Shear (**b**) and unclamping (**c**) stress imparted by the coseismic slip resolved on the afterslip surfaces. In order to eliminate the stress discontinuities on the source rupture, the data are iteratively smoothed by averaging each point with its eight neighbors, as specified in Table 1.

Figure 9. Time series of seismicity beginning 3 months after the Chi-Chi mainshock for (**a**) the East Offshore annulus and (**b**) Miaoli inscribed in Figure 10b.

Figure 10. (**a**) Projected aftershock rate based on the first 3-month decay. The measured p value of Omori decay for each grid is shown. (**b**) Observed seismicity rate change, beginning 15 months after the Chi-Chi earthquake. The cells are 50 x 50 x 30 km for M≥2 earthquakes; this area is needed to contain a sufficient number of earthquakes to solve for p. **(c-d)** Coulomb

stress changes caused by viscoelastic deformation and afterslip 15 months after Chi-Chi resolved on to northwest-striking left-lateral (**c**) and northeast-striking thrust (**d**) faults at 20 km depth. The Coulomb stress at 53 months has the same distribution but is about 15% higher.

Figure 11. Coulomb stress changes and the total seismic moment imparted by (**a**) the modeled Chi-Chi coseismic slip, (**b**) the six M≥6.0 aftershocks occurring during the first 3 months of the mainshock, and (**c**) the modeled afterslip during the 15-month postseismic period.

Table 1

Coseismic shear stress change		Coseismic unclaming stress change	
ramp	décollement	ramp	décollement
5	20	5	10

Table2

No.	Time (year/mo/day)	Latitude deg.	Longitude deg.	Depth km	Strike deg.	Dip deg.	Rake deg.	Coseis. $\Delta\sigma_s$ (bars)	Postseis. $\Delta\sigma_s$ (bars)
1	2001/06/14	24.42	121.93	28	85	48	-25	-0.219	-0.077
2	2001/12/18	23.87	122.65	12	231	56	-9	0.119	0.033
3	2002/05/15	24.65	121.87	17	20	49	167	-0.033	0.006
4	2002/05/28	23.91	122.40	27	312	37	154	0.037	0.077
5	2003/06/09	24.40	121.99	22	225	26	121	-0.027	-0.043
6	2003/06/10	23.52	121.67	29	9	47	66	-0.321	0.065
7	2003/12/10	23.10	121.34	20	23	42	104	-0.058	0.186
8	2004/05/08	21.96	121.49	24	178	28	100	0.011	0.003
9	2004/05/19	22.70	121.39	19	338	39	20	0.093	0.033
10	2004/11/08	23.85	122.58	21	359	30	-140	0.047	0.291
11	2005/03/05	24.67	121.85	19	270	66	-10	-0.107	0.019
12	2005/09/06	23.97	122.23	27	329	34	162	0.027	0.065
13	2006/04/01	22.83	121.12	22	92	70	165	-0.070	0.026
14	2006/04/15	22.85	121.31	18	348	45	52	0.089	0.044

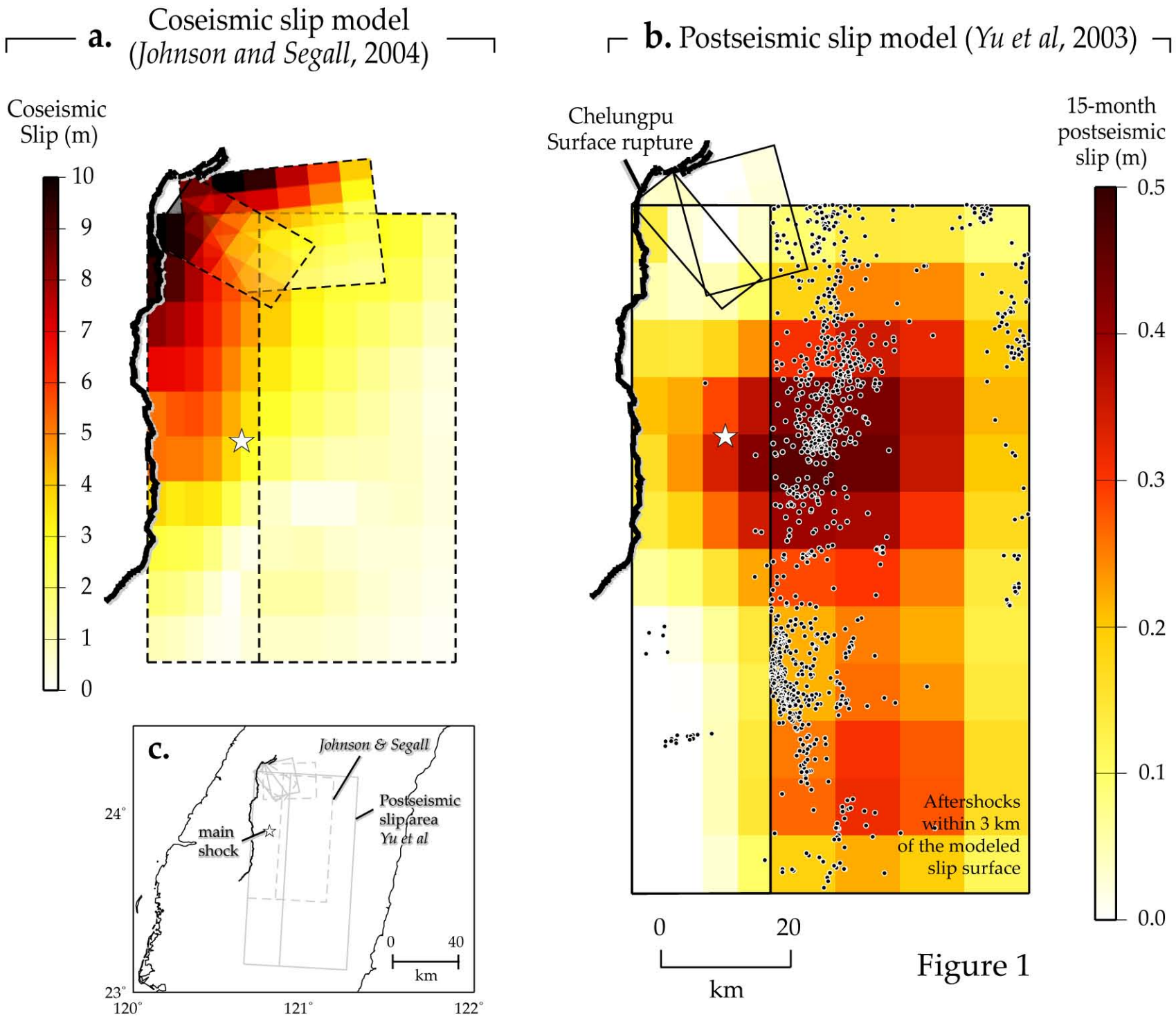
a. Coseismic slip model (Johnson and Segall, 2004)
Coseismic Slip (m)
10
9
8
7
6
5
4
3
2
1
0
b. Postseismic slip model (Yu et al, 2003)
Chelungpu Surface rupture
15-month postseismic slip (m)
0.5
0.4
0.3
0.2
0.1
0.0
Aftershocks within 3 km of the modeled slip surface
0
20
km
c.
Johnson & Segall
Postseismic slip area Yu et al
main shock
24°
23°
120°
121°
122°
0
40
km

Figure 1

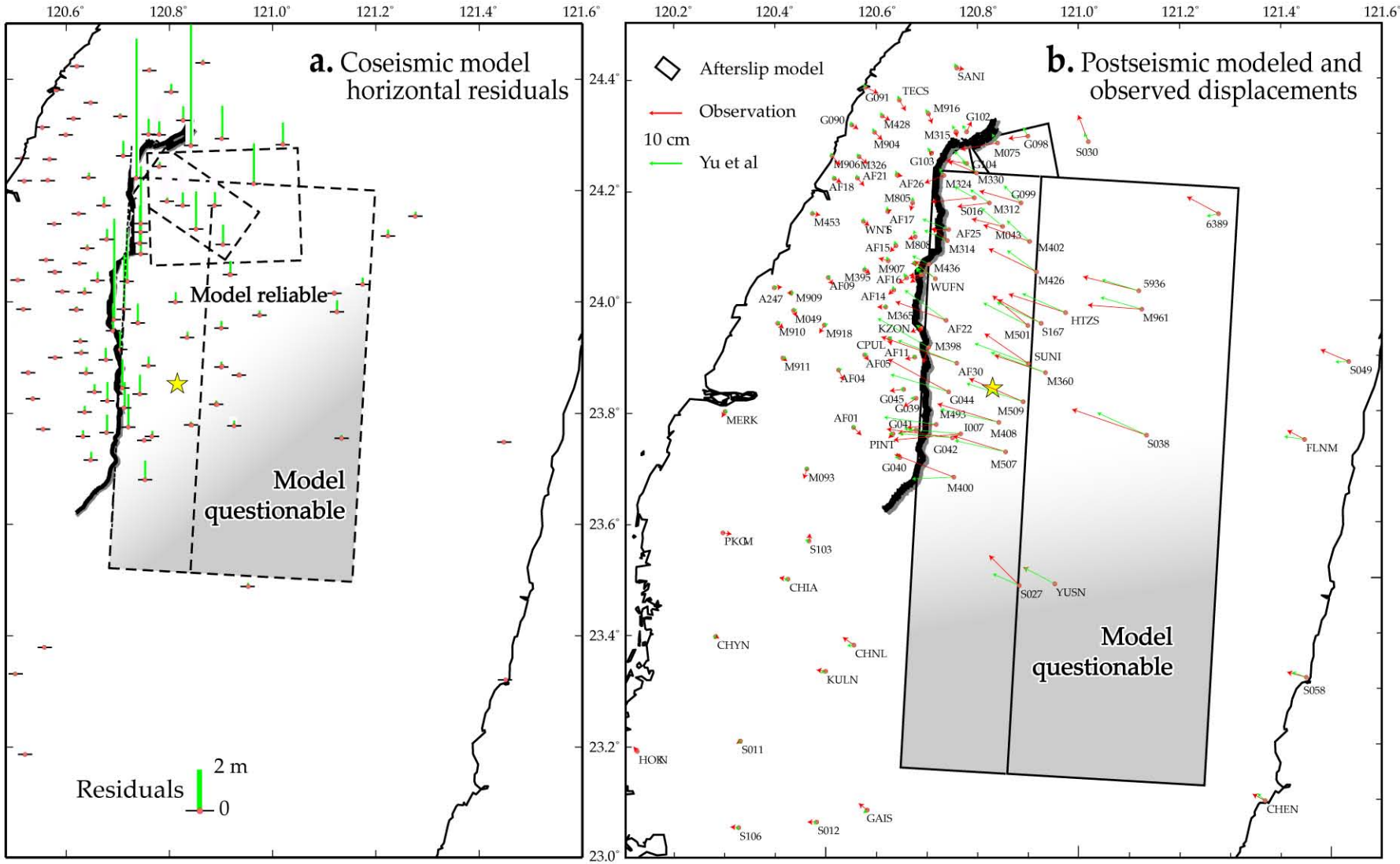
a. Coseismic model horizontal residuals
Model reliable
Model questionable
Residuals
2 m
0
b. Postseismic modeled and observed displacements
Afterslip model
Observation
10 cm
Yu et al
Model questionable
120.6°
120.8°
121.0°
121.2°
121.4°
121.6°
120.2°
120.4°
24.4°
24.2°
24.0°
23.8°
23.6°
23.4°
23.2°
23.0°

Figure 2

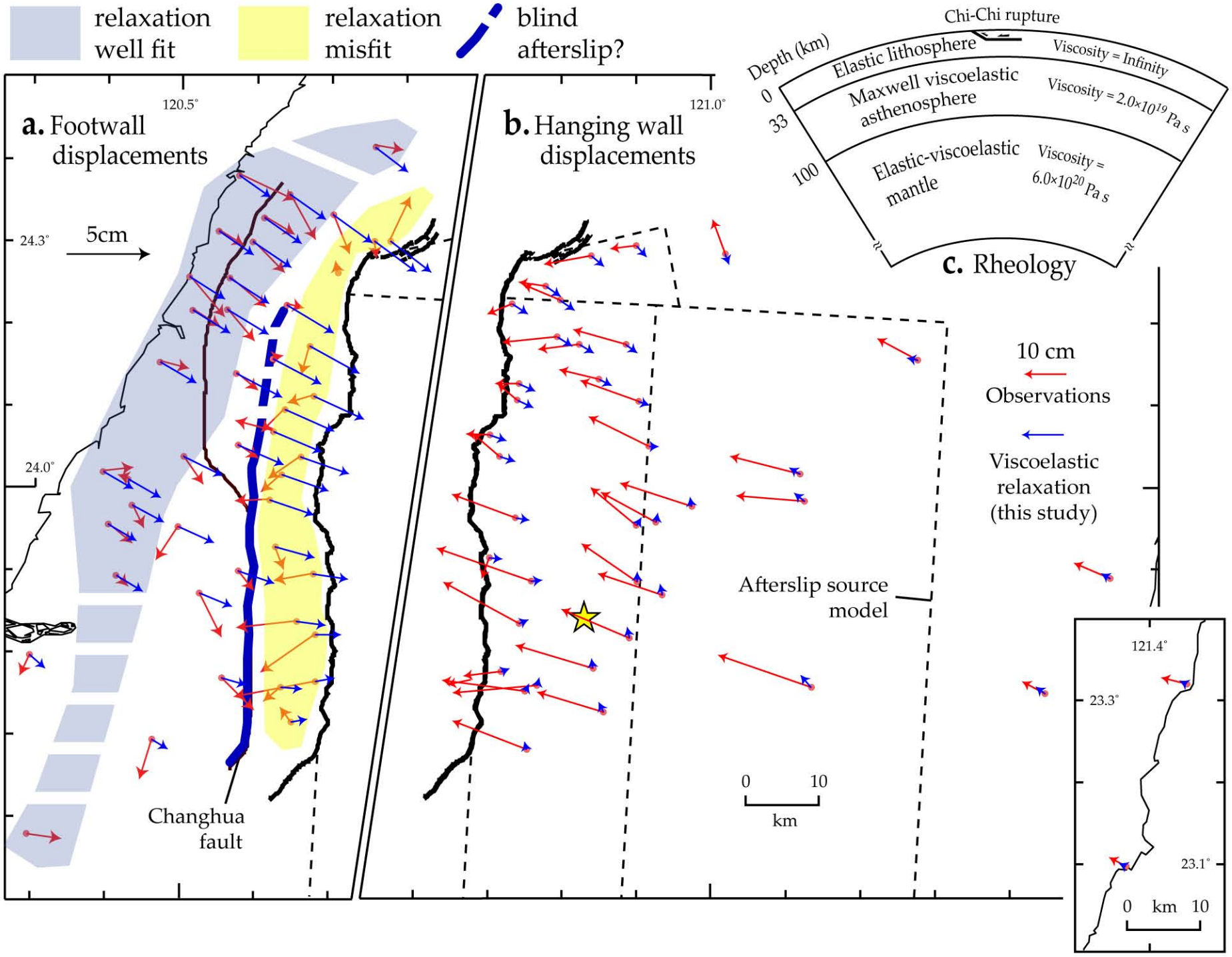
relaxation well fit
relaxation misfit
blind afterslip?
a. Footwall displacements
b. Hanging wall displacements
c. Rheology
Chi-Chi rupture
Depth (km)
0
33
100
Elastic lithosphere
Viscosity = Infinity
Maxwell viscoelastic asthenosphere
Viscosity = 2.0×10^19 Pa s
Elastic-viscoelastic mantle
Viscosity = 6.0×10^20 Pa s
120.5°
121.0°
24.3°
24.0°
5cm
10 cm
Observations
Viscoelastic relaxation (this study)
Afterslip source model
Changhua fault
0
10
km
121.4°
23.3°
23.1°
0 km 10

Figure 3

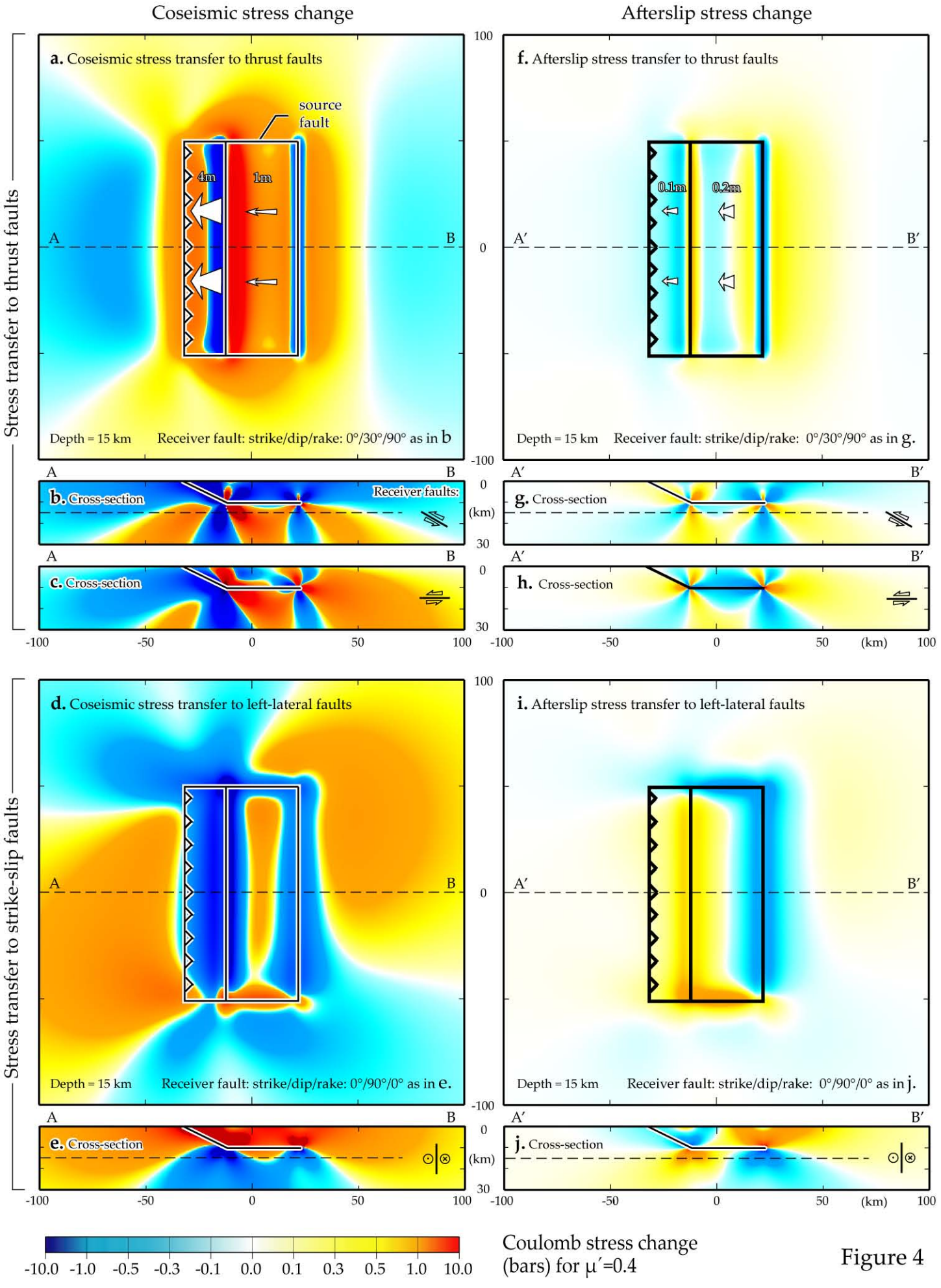
Coseismic stress change
Afterslip stress change
Stress transfer to thrust faults
Stress transfer to strike-slip faults
a. Coseismic stress transfer to thrust faults
source fault
4m
1m
A
B
Depth = 15 km
Receiver fault: strike/dip/rake: 0°/30°/90° as in b
b. Cross-section
Receiver faults:
c. Cross-section
f. Afterslip stress transfer to thrust faults
0.1m
0.2m
A′
B′
Depth = 15 km
Receiver fault: strike/dip/rake: 0°/30°/90° as in g.
g. Cross-section
h. Cross-section
d. Coseismic stress transfer to left-lateral faults
Depth = 15 km
Receiver fault: strike/dip/rake: 0°/90°/0° as in e.
e. Cross-section
i. Afterslip stress transfer to left-lateral faults
Depth = 15 km
Receiver fault: strike/dip/rake: 0°/90°/0° as in j.
j. Cross-section
100
0
-100
30
(km)
-100
-50
0
50
100
-10.0 -1.0 -0.5 -0.3 -0.1 0.0 0.1 0.3 0.5 1.0 10.0
Coulomb stress change (bars) for μ′=0.4

Figure 4

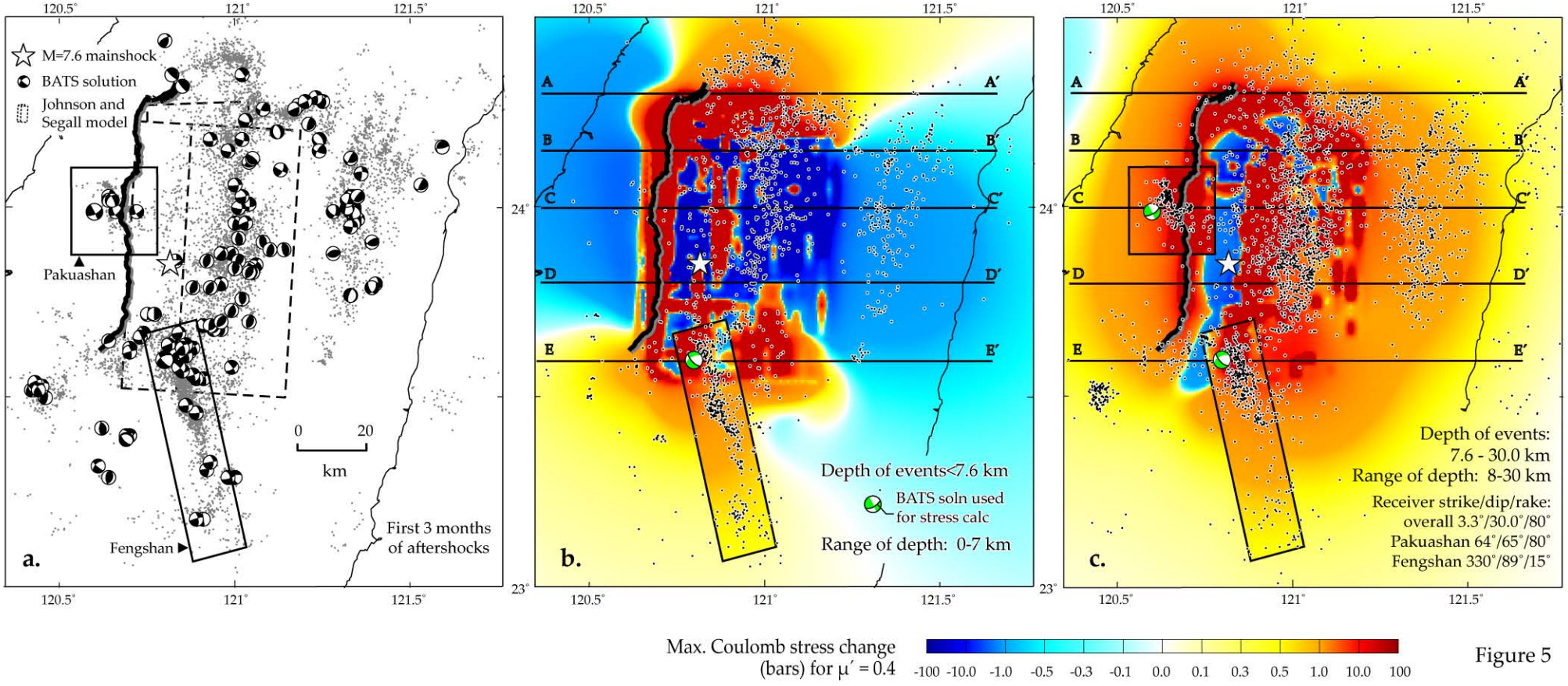
120.5°
121°
121.5°
24°
23°
M=7.6 mainshock
BATS solution
Johnson and Segall model
Pakuashan
Fengshan
0
20
km
First 3 months of aftershocks
a.
A
A′
B
B′
C
C′
D
D′
E
E′
Depth of events<7.6 km
BATS soln used for stress calc
Range of depth: 0-7 km
b.
Depth of events:
7.6 - 30.0 km
Range of depth: 8-30 km
Receiver strike/dip/rake:
overall 3.3°/30.0°/80°
Pakuashan 64°/65°/80°
Fengshan 330°/89°/15°
c.
Max. Coulomb stress change (bars) for μ′ = 0.4
-100 -10.0 -1.0 -0.5 -0.3 -0.1 0.0 0.1 0.3 0.5 1.0 10.0 100

Figure 5

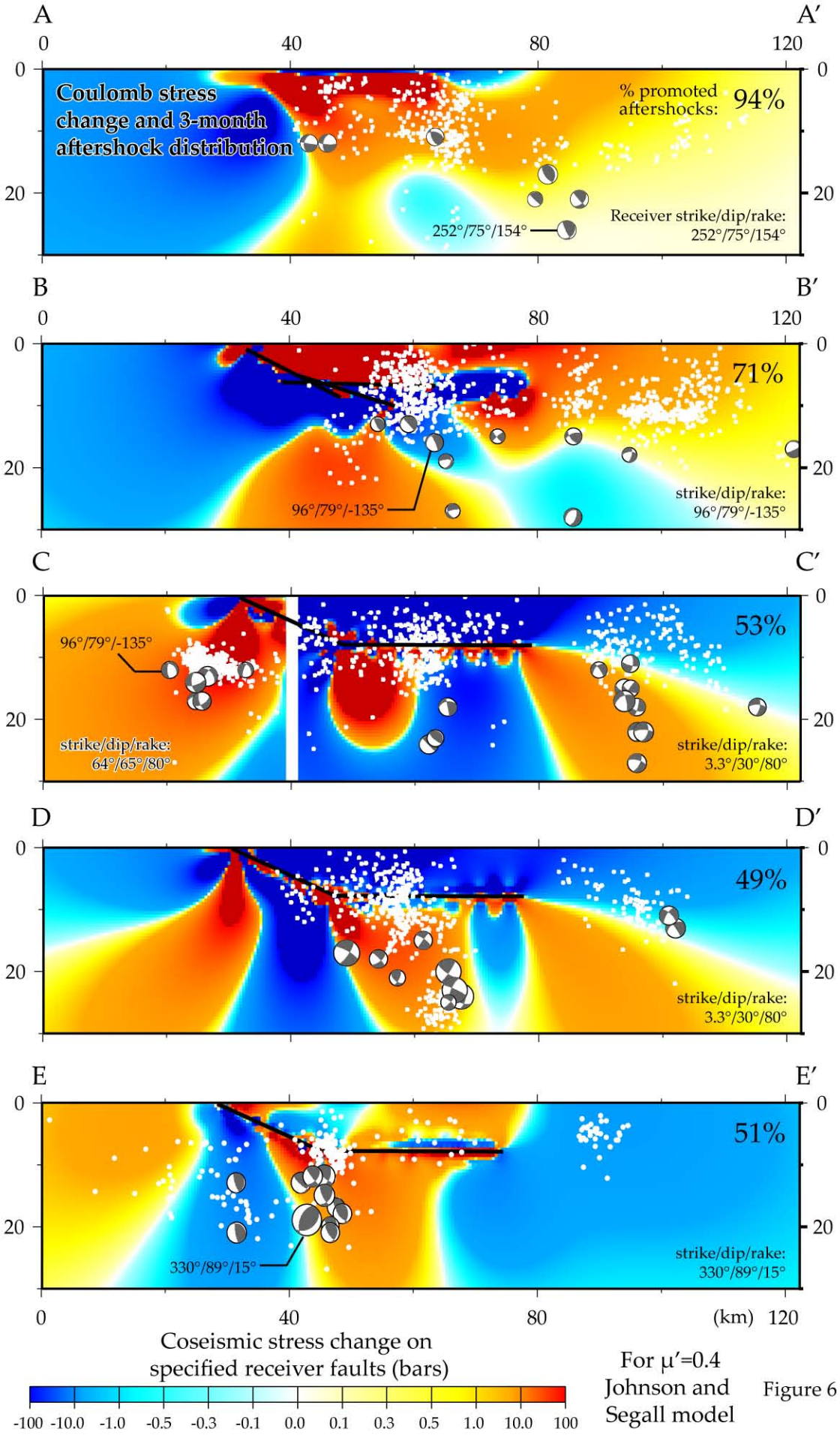

For μ′=0.4 Johnson and Segall model

Figure 6

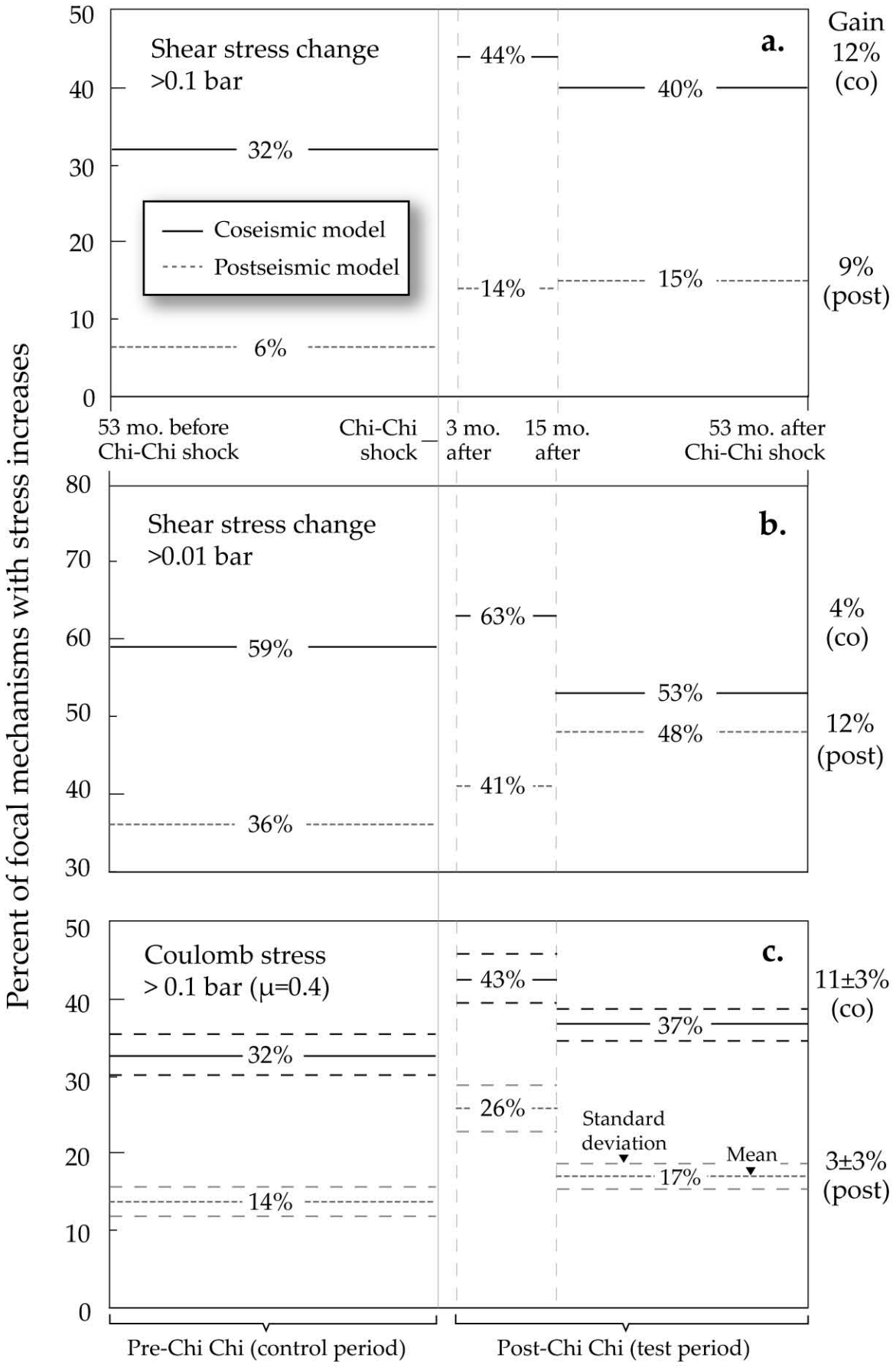
Percent of focal mechanisms with stress increases
Shear stress change
>0.1 bar
a.
Gain
12%
(co)
9%
(post)
Coseismic model
Postseismic model
32%
6%
44%
40%
14%
15%
53 mo. before
Chi-Chi shock
Chi-Chi
shock
3 mo.
after
15 mo.
after
53 mo. after
Chi-Chi shock
Shear stress change
>0.01 bar
b.
4%
(co)
12%
(post)
59%
36%
63%
53%
48%
41%
Coulomb stress
> 0.1 bar (μ=0.4)
c.
11±3%
(co)
3±3%
(post)
32%
14%
43%
37%
26%
17%
Standard
deviation
Mean
Pre-Chi Chi (control period)
Post-Chi Chi (test period)

Figure 7

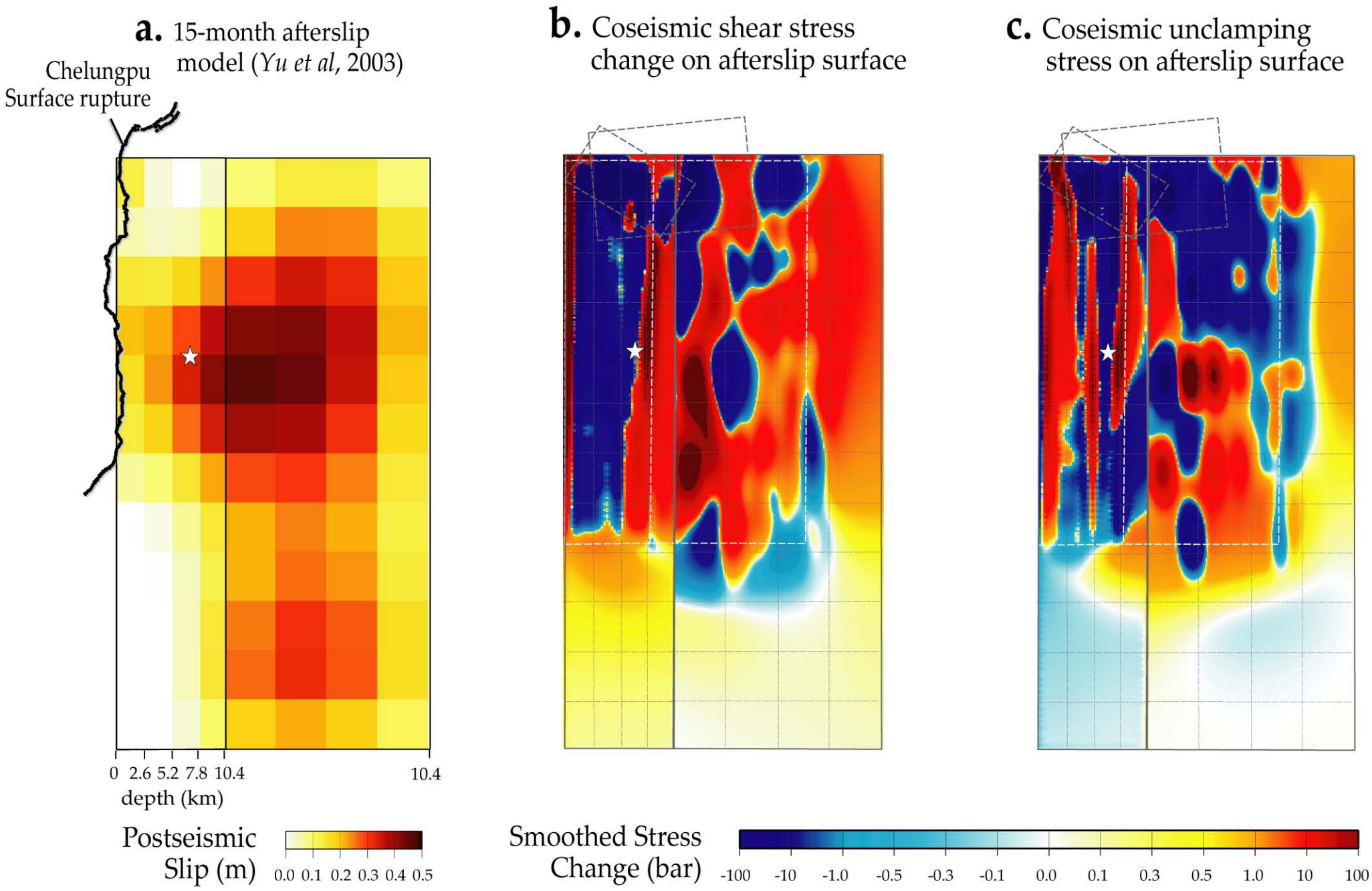
a. 15-month afterslip model (Yu et al, 2003)
Chelungpu Surface rupture
0 2.6 5.2 7.8 10.4
10.4
depth (km)
Postseismic Slip (m)
0.0 0.1 0.2 0.3 0.4 0.5
b. Coseismic shear stress change on afterslip surface
c. Coseismic unclamping stress on afterslip surface
Smoothed Stress Change (bar)
-100 -10 -1.0 -0.5 -0.3 -0.1 0.0 0.1 0.3 0.5 1.0 10 100

Figure 8

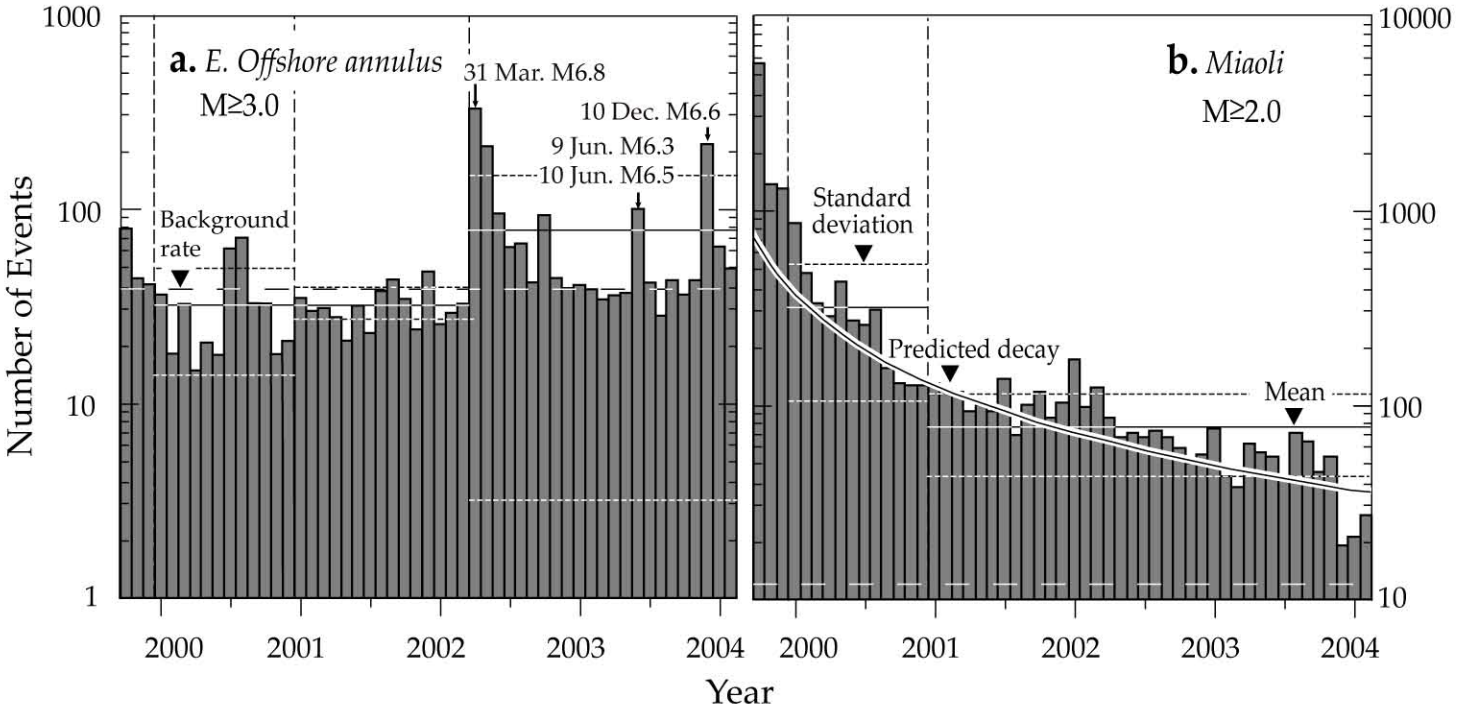
a. E. Offshore annulus
M≥3.0
31 Mar. M6.8
10 Dec. M6.6
9 Jun. M6.3
10 Jun. M6.5
Background rate
b. Miaoli
M≥2.0
Standard deviation
Predicted decay
Mean
Number of Events
Year
1000
100
10
1
10000
1000
100
10
2000
2001
2002
2003
2004

Figure 9

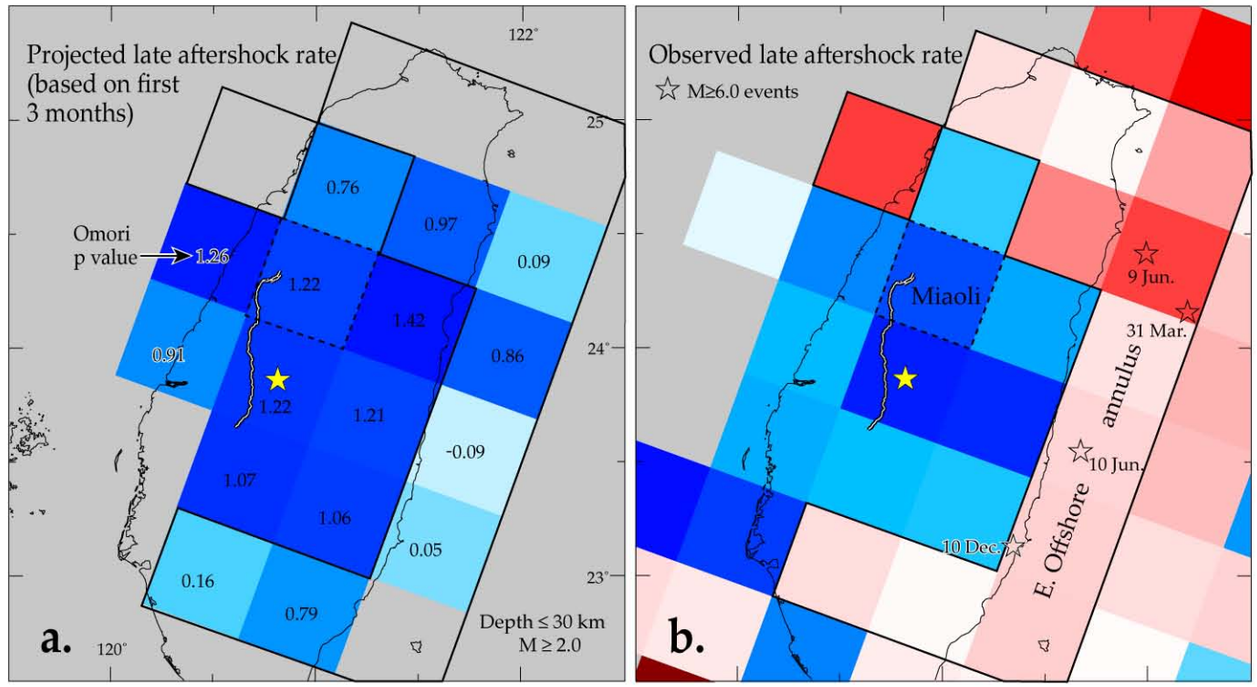
Projected late aftershock rate
(based on first
3 months)
Omori
p value
1.26
0.76
0.97
0.09
1.22
1.42
0.91
0.86
1.22
1.21
-0.09
1.07
1.06
0.05
0.16
0.79
Depth ≤ 30 km
M ≥ 2.0
a.
120°
122°
25°
24°
23°
Observed late aftershock rate
M≥6.0 events
Miaoli
9 Jun.
31 Mar.
10 Jun.
10 Dec.
E. Offshore annulus
b.
0.001 0.01 0.1 0.25 0.33 0.5 1 2 3 4 10 100 1000
Seismicity rate change (15-53 mo. post-Chi Chi divided by 3-15 mo. post-Chi Chi)

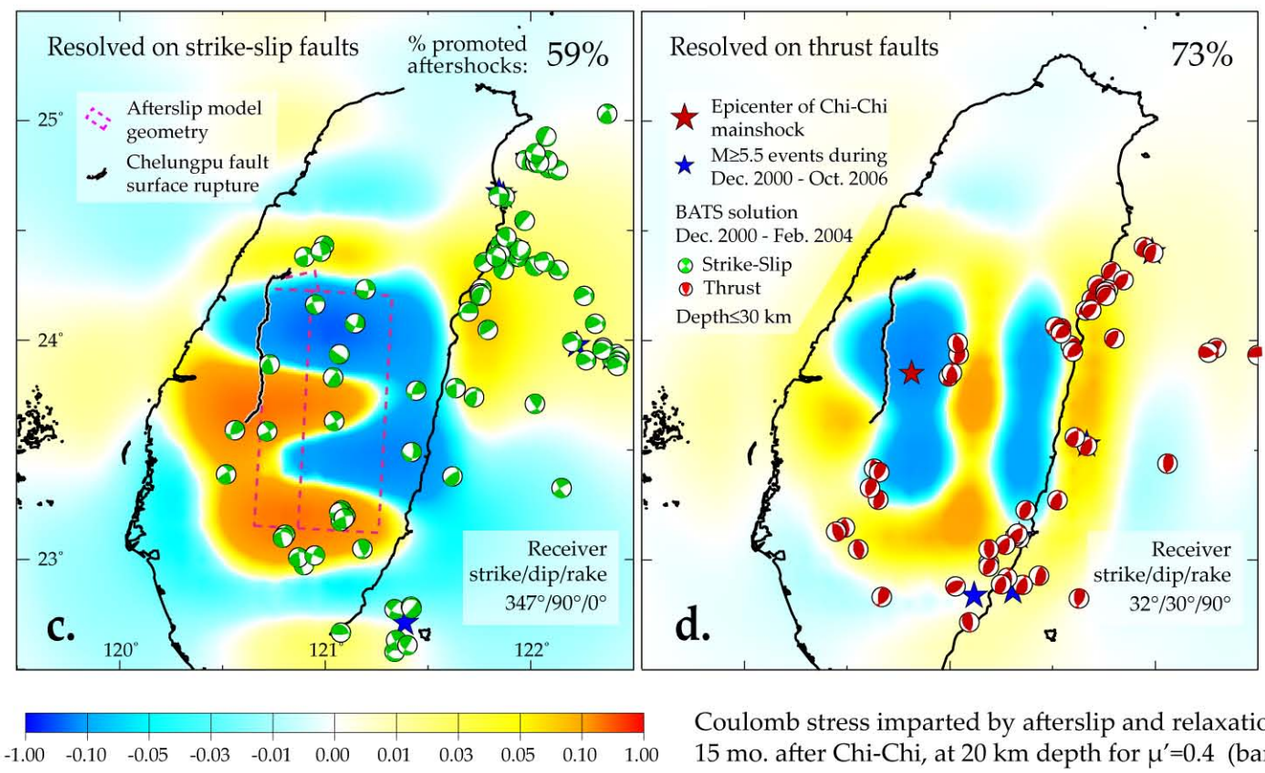
Resolved on strike-slip faults
% promoted aftershocks:
59%
Afterslip model geometry
Chelungpu fault surface rupture
Receiver strike/dip/rake
347°/90°/0°
c.
120°
121°
122°
25°
24°
23°
Resolved on thrust faults
73%
Epicenter of Chi-Chi mainshock
M≥5.5 events during Dec. 2000 - Oct. 2006
BATS solution
Dec. 2000 - Feb. 2004
Strike-Slip
Thrust
Depth≤30 km
Receiver strike/dip/rake
32°/30°/90°
d.
-1.00 -0.10 -0.05 -0.03 -0.01 0.00 0.01 0.03 0.05 0.10 1.00
Coulomb stress imparted by afterslip and relaxation 15 mo. after Chi-Chi, at 20 km depth for μ′=0.4 (bars)

Figure 10

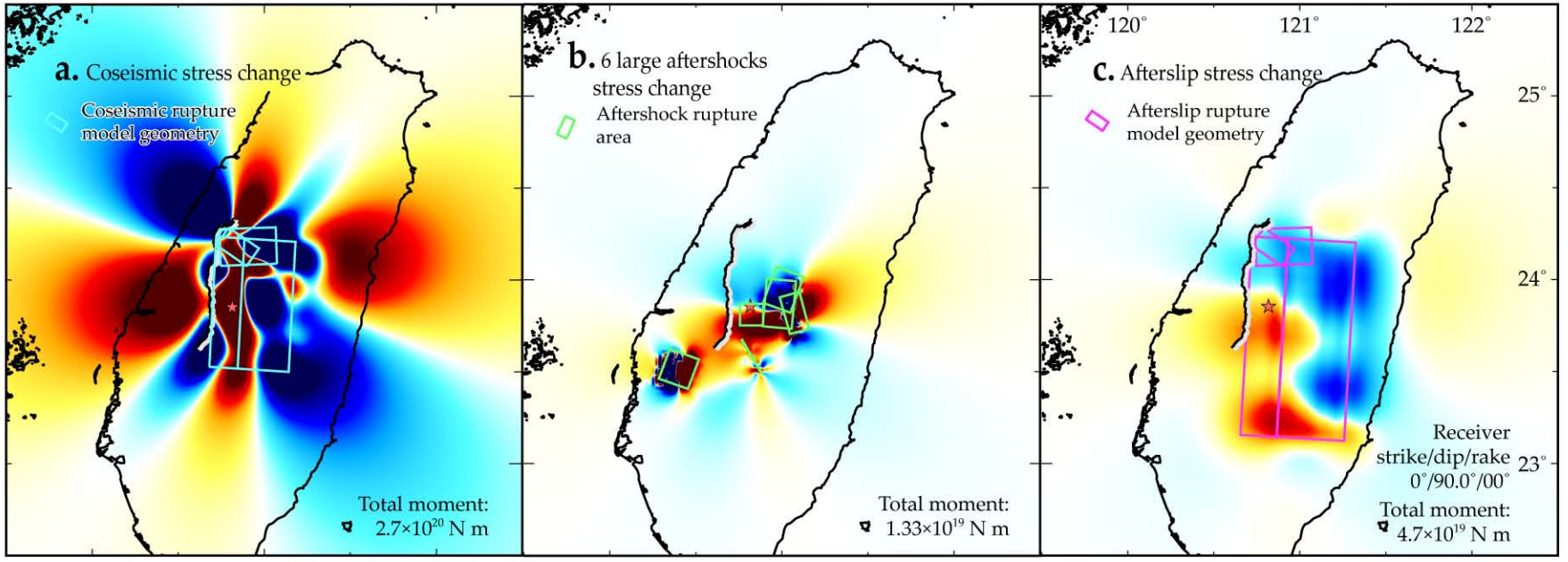
a. Coseismic stress change
Coseismic rupture model geometry
Total moment: 2.7×10^20 N m
b. 6 large aftershocks stress change
Aftershock rupture area
Total moment: 1.33×10^19 N m
c. Afterslip stress change
Afterslip rupture model geometry
120°
121°
122°
25°
24°
23°
Receiver strike/dip/rake 0°/90.0°/00°
Total moment: 4.7×10^19 N m
Coulomb stress change (bars) at 20 km depth for μ′=0.4
-1.0
-0.5
-0.3
-0.1
0.0
0.1
0.3
0.5
1.0

Figure 11